Please cite the Published Version

Additional Information: This is an author accepted manuscript of an article published in Applied Surface Science, by Elsevier.

Data Access Statement: Data will be made available on request.

Amino Modification of Ti_3C_2 MXenes for High-Performance Supercapacitors

Jianbo Wan[1,#], Ruiqing Wu[1,#], Yiyi Chen[1], Hao Zhang[1], Huafeng Li[1], Bohai Wang[1], Tomasz Liskiewicz[2,], Shengwei Shi[1,3,*]*

[1]Hubei Key Laboratory of Plasma Chemistry and Advanced Materials, School of Materials Science and Engineering, Wuhan Institute of Technology, Wuhan, 430205, China
[2]Faculty of Science and Engineering, Manchester Metropolitan University, Manchester M15 6BH, United Kingdom
[3]Key Laboratory of Optoelectronic Chemical Materials and Devices (Ministry of Education), Jianghan University, Wuhan, 430056, China

[#]J. Wan and R. Wu contributed equally to this work.
[*]Email: T.Liskiewicz@mmu.ac.uk (T. Liskiewicz), shisw@wit.edu.cn (S. Shi)

Abstract: MXenes show great potential in energy storage due to their excellent conductivity, abundant surface groups and adjustable interlayer spacing. Amino modification is an effective strategy to improve electrochemical properties of MXene. However, the selection of amino source is still a key issue. Herein, the amino modification of Ti_3C_2 MXenes for high-performance supercapacitors has been investigated. The structure and electrochemical properties of Ti_3C_2 are modified by different amino sources, such as ethylenediamine (EDA), monoethanolamine (MEA) and hydrazine monohydrate (HM). EDA ensures Ti_3C_2 the largest interlayer spacing (13.96 Å) and highest specific surface area (52.2 m^2g^{-1}). In addition, there are more functional groups in EDA-modified Ti_3C_2 (EDA-Ti_3C_2) resulted from the stronger electron-donating nature of EDA than HM and MEA. Thus, EDA-Ti_3C_2 exhibits the largest specific capacitance of 683 F g^{-1} in 1 M H_2SO_4 electrolyte at 2 mV s^{-1}, and the capacitance maintains 97.3% of the original after 10,000 cycles at 50 mV s^{-1}. As a comparison, MEA-Ti_3C_2 and HM-Ti_3C_2 show specific capacitances of 553 F g^{-1} and 470 F g^{-1}, respectively. Furthermore, the symmetric supercapacitor based on EDA-Ti_3C_2 electrode achieves maximum energy density of 7.87 W h kg^{-1} at power density of 600 W Kg^{-1}, and the energy density still remains at 6.34 W h Kg^{-1} even at an increased power density of 3000 W Kg^{-1}. This study proposes a simple strategy to enhance electrochemical properties of MXene by amino modification, providing valuable insights for high-performance supercapacitors.

Keywords: MXenes, amino modification, supercapacitors, specific capacitance

1. Introduction

Two-dimensional (2D) materials possess unique advantages, offering distinctive electrochemical properties and significantly large surface area, which show wide application as electrode materials for high-performance supercapacitors [1]. Since it was firstly synthesized in 2011 [2], 2D MXenes have gained significant attention due to their layered structure and rich surface chemistry, which render MXenes with outstanding hydrophilicity and conductivity, along with excellent mechanical properties and specific capacitances [3]. Up to now, approximately 30 kinds of MXenes have been successfully prepared in laboratory [4], among which Ti_3C_2 is mostly employed with potential applications in various fields, such as supercapacitors[5], sensors[6], catalysis[7], solar cells[8] and flexible electronics[9].

However, there exist some challenges. Hazardous hydrofluoric acid (HF) is generally used in the synthesis of Ti_3C_2, and numerous defects are introduced as well [10]. Indirect fluorination and non-fluorination methods are thus adopted as alternatives to the HF etching, such as chemical vapor deposition[11], electrochemical etching[12] and molten salt etching [13]. The most popular approach is the Minimum Intensity Layering (MILD) method, in which hydrochloric acid (HCl) and lithium fluoride (LiF) are used instead [14]. Zhang *et al* proposed a modified MILD with a Power Focusing Delamination (PFD) strategy [15], and defect-free Ti_3C_2 was obtained with a yield of 61.2% through repeated precipitation and vortex oscillation without ultrasonic process, which exhibited a distinct layered structure. However, the subsequent spontaneous delamination became the challenge due to strong interlayer forces between Ti_3C_2 nanosheets [16]. In addition, Ti_3C_2 was terminated with -OH, -O and -F groups during the etching process, providing abundant active sites for surface modification and the potential introduction of other active groups. However, these surface termination groups only existed in some certain surface areas, which limited the transport of electrolyte ions and thus the electrochemical performance of Ti_3C_2. Several strategies have been employed to modify the structure and properties of Ti_3C_2,

such as intercalation and surface functionalization. Li *et al* improved the pseudocapacitance of Ti_3C_2 through cation intercalation and surface modification, and electrochemical performance of Ti_3C_2 was significantly enhanced with the insertion of K^+ and removal of some terminal groups [17]. Zhang *et al* ingeniously introduced calcium alginate carbonization into Ti_3C_2 nanosheets to form carbon dots, preparing Ti_3C_2 electrodes with high density and more active sites, which demonstrated excellent rate capability (662.5 F cm^{-3} at 1000 A g^{-1}) [18].

The surface chemistry of MXenes plays a crucial role due to their impacts on the properties and performance[19], and different methods have been developed for surface modifications of MXenes, such as plasma activation and alkaline treatment[20–22]. For example, treating MXene surface with alkaline solution to introduce less electronegative -OH groups is found to be an effective method to enhance its electrochemical performance[21]. As -OH termination not only achieves stronger hydrophilicity but also preserves its unique ion-repellent characteristics, which thus significantly reduces ion diffusion resistance during electrochemical reactions and markedly improves the rate capability of the electrode material (from 20.4% to 78.4% at 50 A g^{-1}). Depending on functional groups, MXenes possess extraordinary electronic, mechanical, optical, thermal, and catalytic properties. Even though a variety of properties such as work function, hydrophilic behavior, capacitance, and catalytic activity are ascribed to the surface modification, the structure and composition of the functionalized surfaces remain unknown for most MXenes[23].

Heteroatoms modification, such as nitrogen and sulfur, has been considered to be a facile and effective strategy to improve the specific capacitance, energy density and cycling stability for supercapacitors and metal ion batteries[24–27]. For MXenes, introducing heteroatoms can modify the surface to provide active sites by reducing the quantity of -OH and -F, in addition, heteroatom modification can enlarge the interlayer spacing to hinder the self-stacking of MXene nanosheets, therefore, the electrochemical performance of MXene can be effectively improved. Due to the high electronegativity of nitrogen, it can alter the surface chemistry of carbon-based

electrode materials. Moreover, lone pairs of electrons on nitrogen atoms can easily combine with π electrons on MXene to provide additional pseudocapacitance, and thereby enhance the capacitance of MXene. Moreover, the introduction of nitrogen can suppress the interlayer stacking of MXene by promoting the formation of folding defects and improving mutual repulsion forces, thereby it can expand the interlayer spacing and facilitate the transport of electrolyte ions. Yu *et al* synthesized amino modified MXene/TiO$_2$ heterostructures with cysteine as amino source via a "one-pot method" [28]. This approach integrated several physical and chemical advantages in a complementary and simple manner, exhibiting outstanding electrochemical performance (918.69 F g^{-1} at 0.5 mA cm^{-2}). Yang *et al* effectively enhanced the doping level in MXene (6.3%) by using ammonium citrate as amino source, intercalating agent and antioxidant through a secondary addition of the amino source [29]. The material exhibited a high specific capacitance of 475 F g^{-1} at a current density of 1 A g^{-1} and exceptional stability with 100% capacitance retention after 5000 cycles.

Here, to investigate the influence of different amino sources on the structure and electrochemical properties of Ti$_3$C$_2$, we selected three amino sources with different molecular sizes: ethylenediamine (EDA), monoethanolamine (MEA) and hydrazine monohydrate (HM). Three types of amino-modified Ti$_3$C$_2$ electrodes were prepared through a non-in situ modification. All three amino-modified materials including EDA-Ti$_3$C$_2$, MEA-Ti$_3$C$_2$ and HM-Ti$_3$C$_2$ exhibited porous 2D structure, enhanced hydrophilicity and higher specific surface areas compared with the original Ti$_3$C$_2$. The prepared EDA-Ti$_3$C$_2$ electrode exhibited a high specific capacitance of 683 F g^{-1} in 1 M H$_2$SO$_4$ solution with excellent stability (97.3% capacitance retention after 10,000 cycles). Moreover, the symmetric supercapacitor based on EDA-Ti$_3$C$_2$ electrode achieved a maximum energy density of 7.87 W h Kg^{-1} at a power density of 600 W Kg^{-1}, which can be comparable to those amino-modified carbon-based materials and the original MXene, providing new insights for the development of high-performance supercapacitors.

2. Experimental section

Materials：MAX (Ti$_3$AlC$_2$, purity ≥ 99.9%, 400 mesh) was purchased from Xinxi Technology Co., Ltd. Lithium fluoride (LiF) was provided by Aladdin Reagent Co., Ltd. EDA was obtained from Chengdu Cologne Chemical Co., Ltd. MEA, HM, hydrochloric acid (HCl), sulfuric acid (H$_2$SO$_4$), sodium sulfate (Na$_2$SO$_4$) and ethanol were all purchased from China National Medicines Corp, Ltd.

Preparation of Ti$_3$C$_2$: The preparation of Ti$_3$C$_2$ is based on the MILD method[14]. Initially, 3.2 g of LiF was introduced into a polytetrafluoroethylene reaction vessel containing 40 ml of 9 M HCl. The mixture was then stirred at 500 rpm for 10 minutes to ensure thorough reaction between LiF and HCl. Subsequently, with an ice bath, 2.0 g of Ti$_3$AlC$_2$ was slowly added over 15 minutes to prevent the initial overheating. The reaction was then stirred at 40°C for 72 hours, and the obtained mixture was centrifuged at 5000 rpm for 1 minute to eliminate the residual acid from the etching process. It was then washed with 1 M HCl to purify the MXene, followed by rinsing with deionized water until it reached a neutral pH. Further rinsing with deionized water was continued until the MXene exhibited self-separation. Assisted by a vortex mixer, the precipitated MXene was dispersed, and the dispersion was centrifuged at 3500 rpm for 5 minutes. This process was repeated three times to ensure complete self-expansion of MXene. The obtained precipitated MXene was subjected to ultrasonication for 5 minutes in an ice bath. After centrifugation at 3500 rpm for 30 minutes, the upper layer of the resulting dark-green colloidal solution was collected and labeled as Ti$_3$C$_2$.

Ti$_3$C$_2$ concentration was determined by filtering a known volume through a polytetrafluoroethylene (PTFE) organic micro-porous membrane with a diameter of 50 mm and a pore size of 0.22 μm. Following the determination of Ti$_3$C$_2$ concentration, a specific volume of the Ti$_3$C$_2$ solution was taken. The solution was centrifuged at a speed of 11,000 rpm for 5 minutes to collect a certain mass of precipitated Ti$_3$C$_2$.

Preparation of amino-modified Ti$_3$C$_2$: Amino modification of Ti$_3$C$_2$ was performed by use of three amino sources (EDA, MEA, and HM) with the same doping process. Initially, 30 ml of the amino source was added to the centrifuge tube (50 ml)

containing Ti_3C_2 precipitate. With the help of a vortex mixer, the mixture was shaken for 10 minutes to achieve uniform dispersion. Subsequently, it was transferred to a PTFE reaction vessel (50 ml) and reacted at 40°C with the stirring at 600 rpm for 24 hours in an oil bath. After cooling, the sample was washed three times with ethanol and two times with deionized water in a circulation manner to remove excess amino source reactants. After the final centrifugation, 30 ml of deionized water was added, stirred for 5 minutes, sonicated for 30 minutes in an ice bath, and then vacuum-filtered the solution. The filtered solution was vacuum-dried at 40°C for 12 hours to obtain amino-modified Ti_3C_2 which was named as EDA-Ti_3C_2, MEA-Ti_3C_2 and HM-Ti_3C_2, respectively, for different amino sources used.

Characterizations: The samples were characterized for surface morphology using Field Emission Scanning Electron Microscopy (FESEM, Germany-Zeiss-Ultra plus), Transmission Electron Microscopy (TEM, Japan-JEOL-JEM 2100 F), and Atomic Force Microscopy (AFM). X-ray Diffraction (XRD) patterns were recorded on a Rigaku Smart-Lab SE diffractometer using Cu Kα radiation (λ=0.154178 nm). Fourier Transform infrared spectroscopy (FTIR, Thermo Fisher NICOLET6700) measurements were carried out with the KBr pellet method to analyze the functional groups. The chemical composition and surface terminal groups of the samples were characterized using X-ray Photoelectron Spectroscopy (XPS, USA-Thermo SCIENTIFIC ESCALAB 250Xi). Raman spectroscopy (DXR Raman microscope, excitation wavelength 532 nm) was employed to analyze the composition of the samples. The contact angle of the samples was measured at RT using water as a medium (Germany-Dataphysics-OCA20). The specific surface area and pore size distribution of the samples were determined using the Brunauer-Emmett-Teller (BET) and Barret-Joyner-Halenda (BJH) methods. The electrical conductivity of the samples was measured using a four-probe tester (HP-504).

Electrochemical Measurements: All electrochemical measurements were performed using a CHI660E electrochemical workstation. In a three-electrode cell, cyclic voltammetry (CV), galvanostatic charge-discharge (GCD) and electrochemical impedance spectroscopy (EIS) were conducted. The active material, activated carbon,

and polytetrafluoroethylene (mass ratio 8:1:1) were mixed in N-methyl-2-pyrrolidone (NMP) to form a homogeneous slurry. This slurry was coated onto a copper foam substrate (1 cm×1 cm) and dried in a vacuum oven at 40°C for 12 hours. The coated copper foam was pressed for 30 seconds under a pressure of 10 MPa to obtain the working electrode. Additionally, activated carbon rod and Ag/AgCl were used as the counter and reference electrodes during the testing process. 1 M H_2SO_4 aqueous solution was used as the electrolyte. The specific loading mass is 4.3, 1.3, 1.7 and 2.3 mg/cm^2 for Ti_3C_2, EDA-Ti_3C_2, MEA-Ti_3C_2 and HM-Ti_3C_2, respectively. CV and GCD tests were conducted at different scan rates (2~200 mV s^{-1}) and current densities (1~5 A g^{-1}). EIS spectra were recorded over a frequency range of 100 kHz to 0.01 Hz with perturbation amplitude of 10 mV. Prior to recording the electrochemical performance, 1000 CV scans were performed at a scan rate of 50 mV s^{-1} to stabilize the device.

For the symmetric supercapacitors, the working electrode was placed on either side of a cellulose separator with spacers and springs for support, and was positioned within a battery cap, in which the specific loading mass is 2 mg/cm^2 for both Ti_3C_2 and EDA-Ti_3C_2. It was then thoroughly impregnated with a 1 M Na_2SO_4 as the electrolyte, and finally, the battery was sealed using a coin cell assembly machine under a pressure of 10 MPa.

The specific capacitance in the electrochemical test is calculated from CV (formula 1) and GCD (formula 2).

$$C = \frac{1}{\Delta V} \int \frac{idV}{v} \tag{1}$$

$$C = \frac{i\Delta t}{\Delta V} \tag{2}$$

The energy density (E) （W h kg^{-1}） and power density (P) （W kg^{-1}） can be calculated from formulas (3) and (4), respectively.

$$E = \frac{1}{2 \times 3.6} C \cdot (\Delta V)^2 \tag{3}$$

$$P = \frac{E}{\Delta t} \tag{4}$$

where C represents the specific capacitance, i is the current density, v is the voltage scan rate, V is the voltage, ΔV is the voltage window and Δt is the discharge time.
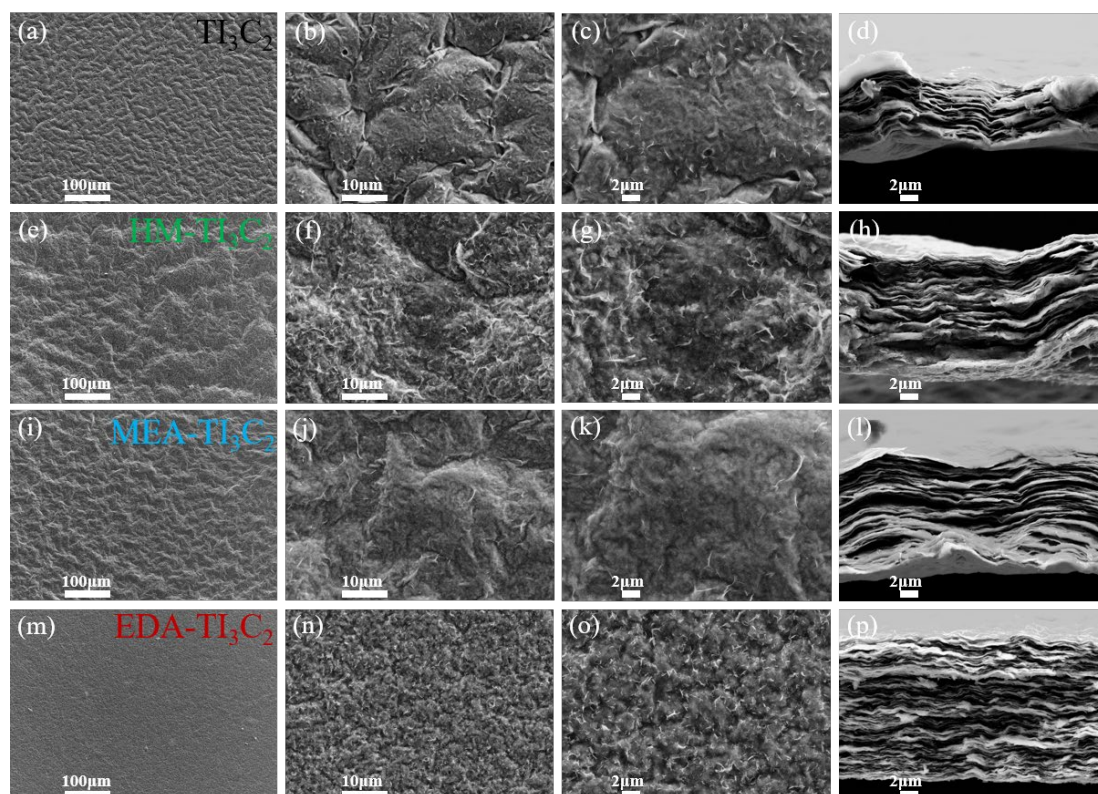
The Coulombic efficiency (CE) can be calculated from the formula (5).

$$CE = \frac{t_d}{t_c} \times 100 \qquad (5)$$

where t_d and t_c are the discharging and charging time in seconds respectively.

3. Results and discussions

FESEM images of top-view and cross-section for Ti_3C_2, $HM\text{-}Ti_3C_2$, $MEA\text{-}Ti_3C_2$ and $EDA\text{-}Ti_3C_2$ are shown in **Figure 1**.

Figure 1. FESEM of top-view images of Ti_3C_2 (a-c), $HM\text{-}Ti_3C_2$ (e-g), $MEA\text{-}Ti_3C_2$ (i-k) and $EDA\text{-}Ti_3C_2$ (m-o) at the same magnification; Cross-sectional images of Ti_3C_2 (d), $HM\text{-}Ti_3C_2$ (h), $MEA\text{-}Ti_3C_2$ (l) and $EDA\text{-}Ti_3C_2$ (p) at the same magnification.

All samples exhibit similar 2D layered structure and the interlayer stacking can be clearly observed in the original Ti_3C_2 (Figure 1d). However, the degree of stacking is alleviated in $HM\text{-}Ti_3C_2$, $MEA\text{-}Ti_3C_2$ and $EDA\text{-}Ti_3C_2$ compared to Ti_3C_2 (Figure 1h, 1l and 1p). It should be indicated that the surface of $EDA\text{-}Ti_3C_2$ demonstrates a more delicate and uniform texture than other samples (Figure 1m, 1n, 1o). In addition, the interlayer spacing in $EDA\text{-}Ti_3C_2$ is obviously enlarged compared to $HM\text{-}Ti_3C_2$ and $MEA\text{-}Ti_3C_2$, and its cross-section indicates great cleanness without protrusions and wrinkles akin to Ti_3C_2 (Figure 1p). From the TEM image of $EDA\text{-}Ti_3C_2$ (Figure S1a),

a distinct layered structure can be observed with the size from 400 nm to several μms. Furthermore, single-layer EDA-Ti$_3$C$_2$ is successfully prepared with the thickness around 2.5 nm from the AFM image (Figure S1b).

Figure 2 gives XRD patterns for Ti$_3$C$_2$, HM-Ti$_3$C$_2$, MEA-Ti$_3$C$_2$ and EDA-Ti$_3$C$_2$, and all patterns are similar to previous reports[5]. Amino-modified Ti$_3$C$_2$ samples only exhibit the main (002) peak, indicating successful removal of Al layers during the etching process. Figure 2b shows the shift in the position of (002) peak for different Ti$_3$C$_2$, indicating the effect of amino modification on interlayer spacing. The interlayer spacing (d) can be calculated according to Bragg's equation (Formula 6).

$$2d\sin\theta = n\lambda \tag{6}$$
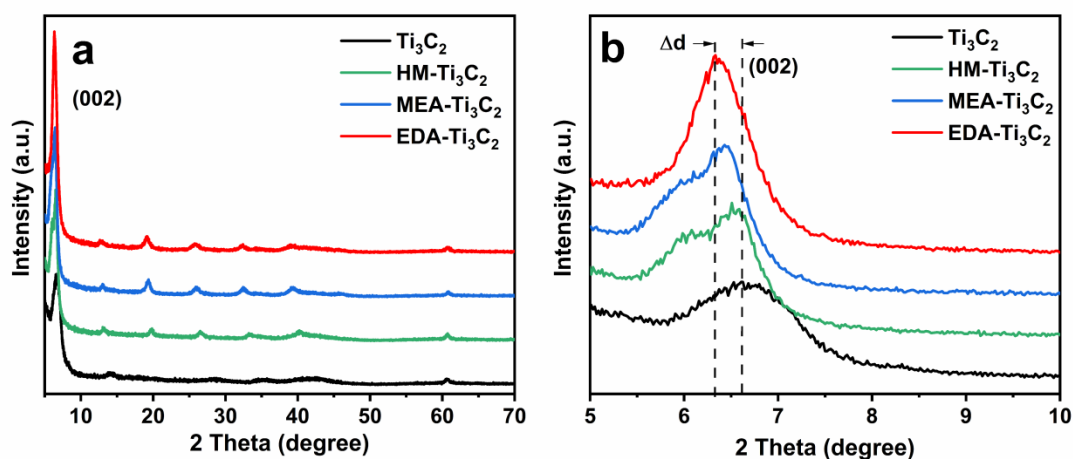
**Figure 2.** XRD patterns (a) and diffraction peaks near the (002) crystal plane (b) for Ti$_3$C$_2$, HM-Ti$_3$C$_2$, MEA-Ti$_3$C$_2$ and EDA-Ti$_3$C$_2$.

Table 1. Structural parameters from XRD

Sample	2θ (degree)	d spacing (Å)
Ti$_3$C$_2$	6.62	13.35
HM-Ti$_3$C$_2$	6.50	13.59
MEA-Ti$_3$C$_2$	6.43	13.74
EDA-Ti$_3$C$_2$	6.33	13.96

Table 1 summarizes the specific position of the (002) peak and corresponding interlayer spacing. It can be observed that the 2θ value decreases with the amino modification. EDA-Ti$_3$C$_2$ shows the smallest 2θ at 6.33°, followed by MEA-Ti$_3$C$_2$ at 6.43° and HM-Ti$_3$C$_2$ at 6.50°, and Ti$_3$C$_2$ has the largest 2θ at 6.62°. Thus, EDA-Ti$_3$C$_2$ exhibits the largest interlayer spacing of 13.96 Å, and it is 13.74 Å and 13.59 Å for MEA-Ti$_3$C$_2$ and HM-Ti$_3$C$_2$, respectively. While Ti$_3$C$_2$ shows the smallest interlayer

spacing of 13.35 Å. The results indicate that the introduction of amino can effectively enlarge the distance between nanosheets of Ti_3C_2, preventing the self-stacking of Ti_3C_2, which is well consistent to results in Figure 1. However, there is no much difference in the interlayer spacing among EDA-Ti_3C_2, MEA-Ti_3C_2 and HM-Ti_3C_2, which may be due to the similar molecular size for HM, MEA and EDA. The largest interlayer spacing of EDA-Ti_3C_2 may provide more Ti_3C_2 surface for electrochemical reaction, facilitating more H^+ ions (with a radius of 1.2 Å) to participate in the reaction during the rapid charge-discharge process[30]. Therefore, amino modification is expected to enhance the electrochemical performance of Ti_3C_2.
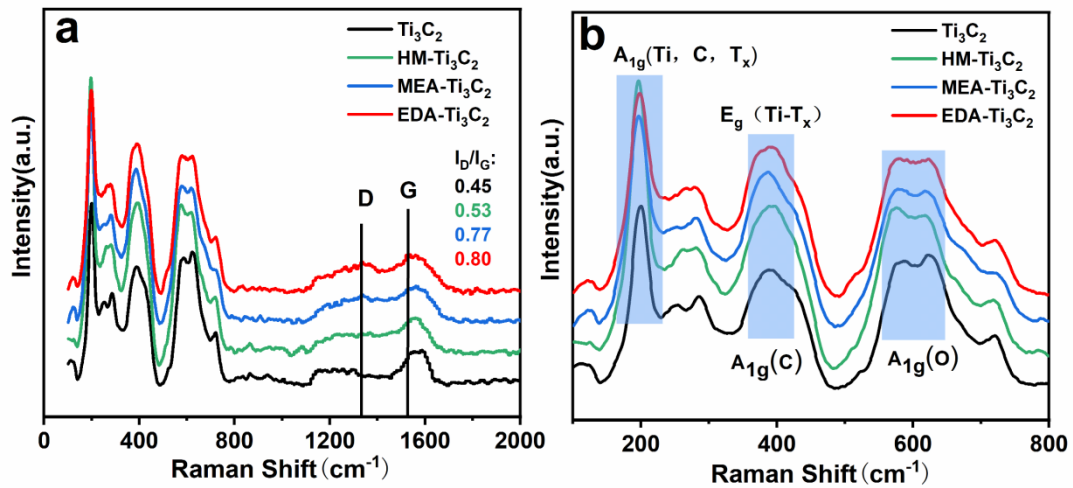
Figure 3. Raman spectra under the excitation of a 532 nm laser. (a) 100-2000 cm^{-1} and (b) 100-800 cm^{-1}.

Raman spectra can provide rich information about the stacking, surface chemistry and quality of Ti_3C_2, and it can also be used to analyze surface functional groups. **Figure 3** shows Raman spectra under the excitation of a 532 nm laser for all samples, and the peak positions are consistent to the reported before [5,31]. In the range of 100-800 cm^{-1}, A strong vibration feature at $\sim$200 cm^{-1} is related to the A_{1g} (Ti, C and O) mode, the out-of-plane vibration in MXene nanosheets. For this feature, Raman shifts for Ti_3C_2, HM-Ti_3C_2, MEA-Ti_3C_2 and EDA-Ti_3C_2 are 200.6, 197.2, 197.4 and 197.4 cm^{-1}, respectively, and different Raman shifts are attributed to their intercalation effects. The Raman shift decreases with the increasing interlayer spacing. Comparing with Ti_3C_2, there is a 3 cm^{-1} Raman shift as amino sources are used. Furthermore, wide features at 230−470 cm^{-1} are generally attributed to a mixture of in-plane E_g (Ti−

T_x) and out-of plane A_{1g} (C) vibration modes, which are related to functional groups attached to Ti atoms [5,32]. The main feature of in-plane E_g (Ti−T_x) vibration is observed from 360 to 460 cm^{-1}, and the A_{1g} (C) vibration is also situated in this region resulting from the attachment of C atoms to Ti and other terminal groups. The E_g (Ti−T_x) features are found to be located at 394.3, 391.3, 388.4 and 386.8 cm^{-1} for Ti_3C_2, HM-Ti_3C_2, MEA-Ti_3C_2 and EDA-Ti_3C_2, respectively. Furthermore, the features at 580 cm^{-1} were attributed to the A_{1g} vibration of O atoms. In the range of 1000-1800 cm^{-1}, two peaks at 1560 and 1340 cm^{-1} could be observed for all samples. The peak at 1340 cm^{-1} (D-band) is associated with disordered graphite structure resulted from defects and disorders in carbon-based materials, while the peak at 1560 cm^{-1} (G-band) is attributed to the vibration of sp2 hybridized carbon atoms in a 2D hexagonal lattice [33], which is consistent to 2D structure of from the TEM in **Figure S1**. The intensity ratio of D to G band (I_D/I_G) depends on the type of graphitic structure and reflects the graphitization degree. EDA-Ti_3C_2 exhibits the highest I_D/I_G of 0.80, which may be due to more disordered structure and defects in EDA-Ti_3C_2. In addition, D and G bands shift towards higher wavelength with amino modification, indicating the restoration of conjugated structures following the incorporation of nitrogen elements into the Ti_3C_2 lattice [34].

The N_2 adsorption-desorption isotherms (BET) for Ti_3C_2, HM-Ti_3C_2, MEA-Ti_3C_2, and EDA-Ti_3C_2 are shown in **Figure 4**. All samples exhibit typical type IV isotherms, with hysteresis loops characteristic of H3 type [35]. The relevant pore structure related parameters are presented in **Table 2**. The specific surface area of Ti_3C_2 increases with amino modification. As indicated in XRD results (Figure 2), the enlargement of interlayer spacing allows Ti_3C_2 to generate more effective reaction space. Here, EDA-Ti_3C_2 exhibits the largest specific surface area (52.2 m^{2}g^{-1}), representing an increase of more than 200% compared to Ti_3C_2 (16.7 m^{2}g^{-1}), and that is 38.9 m^{2}g^{-1} and 27.4 m^{2}g^{-1} for MEA-Ti_3C_2 and HM-Ti_3C_2, respectively. Furthermore, the pore size distribution in Figure 4b indicates that EDA-Ti_3C_2 primarily features mesoporous structures (2-50 nm), and the high BET surface area facilitates sufficient contacts between electrode materials and H$^+$ during the

electrochemical reaction. This enhances the efficiency of electrolyte ion transport and diffusion, leading to more thorough reactions and improved electrochemical performance of supercapacitors [36].
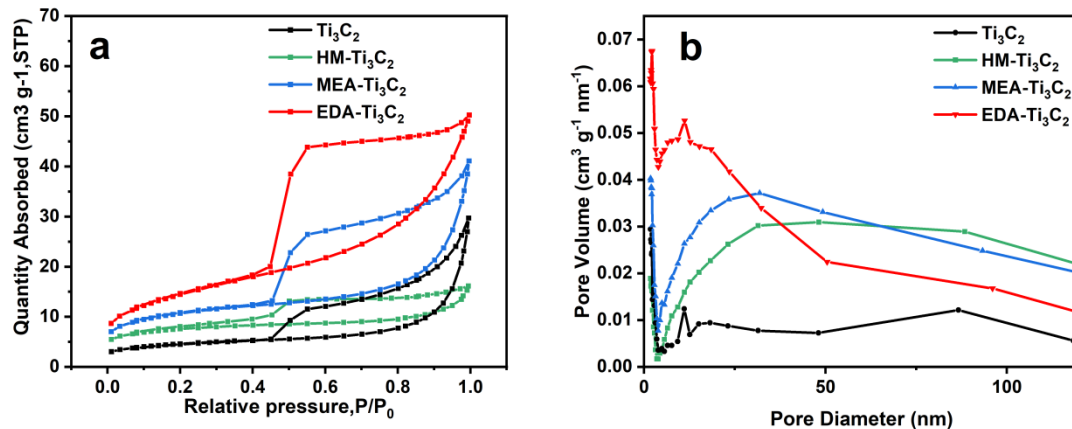
Figure 4. Nitrogen adsorption-desorption isotherms (a) and pore size distribution (b) for Ti_3C_2, $HM-Ti_3C_2$, $MEA-Ti_3C_2$ and $EDA-Ti_3C_2$.

Table 2. BET results for all samples.

Sample	$S_{BET}(m^2 \, g^{-1})$	$V_{pore}(cm^3 \, g^{-1})$
Ti_3C_2	16.7	0.021
$HM-Ti_3C_2$	27.4	0.018
$MEA-Ti_3C_2$	38.9	0.040
$EDA-Ti_3C_2$	52.2	0.062

To gain insights into the hydrophilicity of amino-modified Ti_3C_2, contact angle measurements were conducted as shown in **Figure S2**. $EDA-Ti_3C_2$ shows the smallest contact angle of 48°, representing a reduction of 31° compared to Ti_3C_2 (79°), and it also decrease to 73° and 71° for $MEA-Ti_3C_2$ and $HM-Ti_3C_2$, respectively. The small contact angle endows the good infiltration between MXene and electrolytes. This improvement in the hydrophilicity may be attributed to the presence of more oxygen-containing functional groups on their surfaces, as confirmed by XPS results later.

In addition, the electrical conductivity of Ti_3C_2 has been measured (**Figure S3**). The sheet resistance is 0.22 Ω sq^{-1} for Ti_3C_2, and it slightly increases to 0.41 Ω sq^{-1}, 0.55 Ω sq^{-1} and 1.1 Ω sq^{-1} for $HM-Ti_3C_2$, $MEA-Ti_3C_2$ and $EDA-Ti_3C_2$, respectively. Correspondingly, the electrical conductivity shows a small reduction from 2155 S cm^{-1} for Ti_3C_2 to 1243 S cm^{-1}, 1173 S cm^{-1} and 239 S cm^{-1} for $HM-Ti_3C_2$, $MEA-Ti_3C_2$ and $EDA-Ti_3C_2$, respectively. The interlayer spacing in Ti_3C_2 is expanded due to the amino modification, resulting in more discontinuous structures, and more surface-

exposed Ti undergoes oxidization, thus the electrical conductivity is reduced to some extent. However, the electrical conductivity of amino-modified Ti_3C_2 is still reasonable for the electrode material in supercapacitors. In addition, the enlargement of interlayer spacing is beneficial to electrolyte ion transport and diffusion during the charging/discharging process. Therefore, amino modification can effectively improve electrochemical performance of Ti_3C_2.
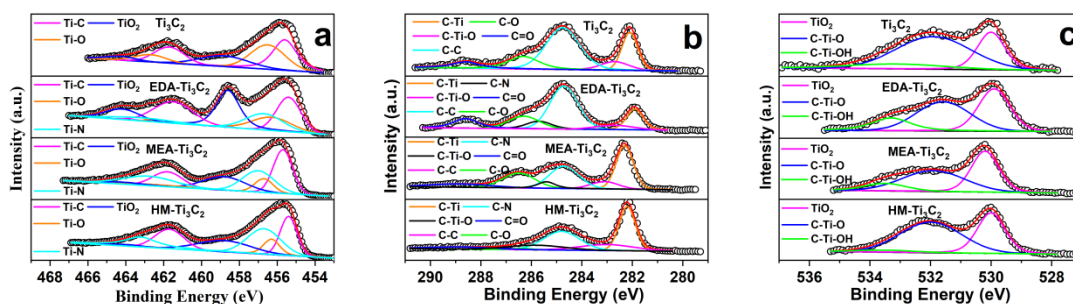
Figure S4 gives FTIR for Ti_3C_2, $HM-Ti_3C_2$, $MEA-Ti_3C_2$ and $EDA-Ti_3C_2$. The narrow and strong feature of -OH around 3409 cm^{-1} in Ti_3C_2 can be observed, and as the introduction of amino groups, the wide feature of -NH around 3450 cm^{-1} appears, which is mixed with the one from -OH. In addition, we can find the δ_{N-H} around 1620 cm^{-1}. Furthermore, the intensity of C-F is reduced in amino-modified Ti_3C_2. Thus we can confirm the successful modification of amino in MXenes, which partially replaced -F in the surface of MXenes.
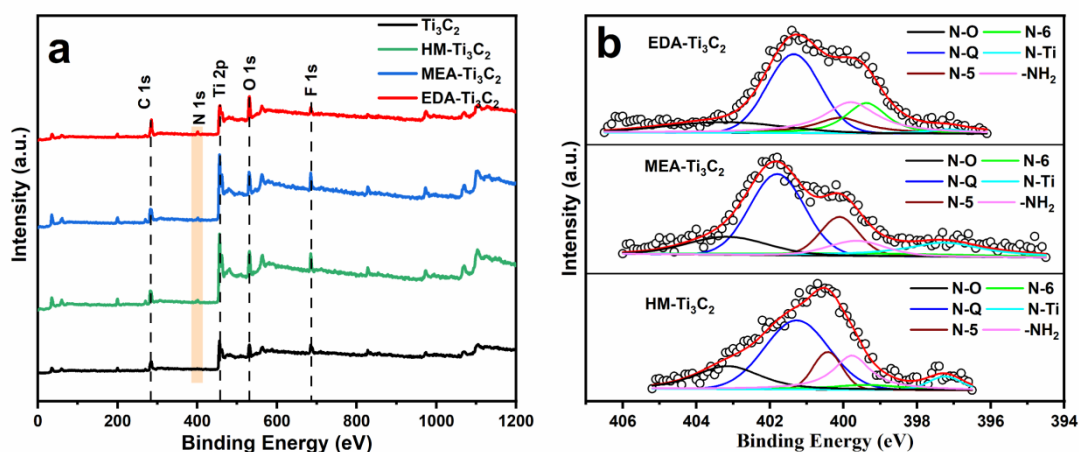
Figure 5. XPS survey scan (a) and N 1s (b) for Ti_3C_2, $HM-Ti_3C_2$, $MEA-Ti_3C_2$ and $EDA-Ti_3C_2$.

Figure 5 presents XPS spectra for Ti_3C_2, $HM-Ti_3C_2$, $MEA-Ti_3C_2$ and $EDA-Ti_3C_2$. In the survey scan, major features are displayed corresponding to C 1s, N 1s, Ti 2p, O 1s and F 1s. **Table S1** list element contents in various Ti_3C_2, and it can be observed that $EDA-Ti_3C_2$ has the nitrogen content of 3.93%, which is much higher than that in $HM-Ti_3C_2$ (2.75%) and $MEA-Ti_3C_2$ (2.78%), respectively. $EDA-Ti_3C_2$ also exhibits the lowest fluorine content of 5.77%, much lower than $HM-Ti_3C_2$ (9.72%) and $MEA-Ti_3C_2$ (8.67%), respectively. The nitrogen may replace a considerable portion of -F in the surface of Ti_3C_2 [30]. N 1s spectra in Figure 5b reveal five features for EDA-

Ti$_3$C$_2$: nitrogen oxide (N-O, 403.23 eV, 11.41%), quaternary nitrogen (N-Q, 401.35 eV, 38.29%), pyrrolic nitrogen (N-5, 400.09 eV, 10.52%), pyridinic nitrogen (N-6, 399.38 eV, 15.00%), nitride (N-Ti, 397.13 eV, 2.24%) and amino (-NH$_2$, 399.8, 22.54%) [36]. **Table S2** lists the detailed analysis of N 1s. The results indicate that beside the amino group, the partial nitrogen combines with carbon in the carbon lattice of Ti$_3$C$_2$ layers to form C-N bonds (N-Q, N-5, N-6), while the remaining nitrogen replaces carbon to form N-Ti bonds. The N-O bonds may be due to partial oxidation of Ti$_3$C$_2$ during the doping process. Compared to HM-Ti$_3$C$_2$ and MEA-Ti$_3$C$_2$, EDA-Ti$_3$C$_2$ shows the highest content of amino groups, relatively high content of N-6 and N-Q, while with the least content of N-5, N-O and N-Ti. As EDA has good nitrogen migration due to its better electron-donating nature than HM-Ti$_3$C$_2$ and MEA-Ti$_3$C$_2$, and it can combine with Ti$_3$C$_2$ surface more effectively, therefore, N-Q becomes the predominant type (38.29%) in EDA-Ti$_3$C$_2$. In addition, suitable temperature and sufficient stirring speed promote the formation of high-energy N-Q and transform unstable N-5 (10.52%) into more stable N-6 (15.00%). Moreover, N-6 provides electron pairs in conjugation with π orbitals, therefore, EDA-Ti$_3$C$_2$ exhibiting the electron-donating characteristic, which is beneficial to high capacitance. In addition, N-O bonds may adversely affect the electrochemical performance by reducing active reaction sites, resulting in decreased capacitance, while N-Ti bonds are considered to contribute less to the overall process [37].

Figure 6. High-resolution XPS of Ti 2p (a), C 1s (b) and O 1s (c) for Ti$_3$C$_2$, HM-Ti$_3$C$_2$, MEA-Ti$_3$C$_2$, and EDA-Ti$_3$C$_2$.

To further investigate the distribution of surface functional groups, high-resolution XPS is performed on Ti 2p (**Figure 6a**). Two main features correspond to Ti 2p1/2

and Ti 2p3/2. In Ti$_3$C$_2$, these include the main Ti-C (455.42 eV, 461.5 eV), surface Ti-O (456.7 eV, 462.7 eV) and O-Ti-O (459 eV, 464.2 eV). The features for EDA-Ti$_3$C$_2$ are Ti-C (455.4 eV, 461.5 eV), Ti-O (456.3 eV, 462.8 eV) and O-Ti-O (458.6 eV, 464.2 eV) with the new appearance of Ti-N (456.7 eV, 463.2 eV). Besides the emerged Ti-N, the O-Ti-O in EDA-Ti$_3$C$_2$ is different from Ti$_3$C$_2$ with stronger intensity. While, MEA-Ti$_3$C$_2$ and HM-Ti$_3$C$_2$ show no significant difference in the features other than Ti-N bond. For MEA-Ti$_3$C$_2$, the main features correspond to Ti-C (455.7 eV, 461.8 eV), Ti-O (456.7 eV, 462.5 eV), O-Ti-O (458.8 eV, 464.2 eV) and Ti-N (457.0 eV, 462.8 eV). For HM-Ti$_3$C$_2$, they are Ti-C (455.4 eV, 461.7 eV), Ti-O (456.3 eV, 462.8 eV), O-Ti-O (458.8 eV, 464.0 eV) and Ti-N (456.7, 463.2 eV). The detailed analysis of Ti 2p is given in **Table S3**, and the Ti-N confirms the successfully amino modification. The polarity of Ti-N bond is beneficial to the adsorption capacity for H$^+$ on electrode surface during the electrochemical reaction.

The C 1s spectra are shown in Figure 6b. In Ti$_3$C$_2$, there are five main features at 282.1, 282.7, 284.75, 286.3, and 288.6 eV, corresponding to C-Ti, C-Ti-O, C-C, C-O and C=O, respectively. With the amino modification, additional C-N bond appears. For HM-Ti$_3$C$_2$, the peaks are at 282.2, 283, 284.8, 285.8, 286.4, and 288.8 eV, corresponding to C-Ti, C-Ti-O, C-C, C-N, C-O and C=O. Similarly, MEA-Ti$_3$C$_2$ exhibits corresponding peaks at 282.3, 283.1, 284.7, 285.4, 286.5, and 288.8 eV. EDA-Ti$_3$C$_2$ shows characteristic peaks at 281.9, 282.7, 284.7, 285.7, 286.3, and 288.6 eV. From **Table S4**, it can be observed that C-Ti bond shifts from 282.1 eV to a lower binding energy of 281.9 eV in EDA-Ti$_3$C$_2$. For C-Ti-O bond, its binding energy increases from 282.7 eV in Ti$_3$C$_2$ to 283 eV and 283.1 eV in HM-Ti$_3$C$_2$ and MEA-Ti$_3$C$_2$, respectively, and the content of C-Ti-O bond also increases especially in HM-Ti$_3$C$_2$, while it remains the same as Ti$_3$C$_2$ in EDA-Ti$_3$C$_2$, and the content shows the lowest in all Ti$_3$C$_2$, indicating that more oxidization of Ti in HM-Ti$_3$C$_2$ and MEA-Ti$_3$C$_2$ than that in EDA-Ti$_3$C$_2$.

As shown in Figure 6c, O 1s mainly includes three characteristic features: TiO$_2$, C-Ti-O and C-Ti-OH[38], which are located at 530, 531.9, and 533.1 eV, respectively for Ti$_3$C$_2$. For all amino-modified Ti$_3$C$_2$, they exhibit nearly the similar O 1s with

Ti$_3$C$_2$, only different in their contents. **Table S5** lists the detailed analysis of O 1s. It can be observed that the content of TiO$_2$ increases in amino-modified Ti$_3$C$_2$, which means that oxidization happens during the amino modification. In addition, the highest content of C-Ti-OH shows more functional groups (-OH) in EDA-Ti$_3$C$_2$ than HM-Ti$_3$C$_2$ and MEA-Ti$_3$C$_2$. Furthermore, all Ti$_3$C$_2$ exhibit the highest content of the main feature of C-Ti-O, which means that the presence of -O functional groups on the surface.
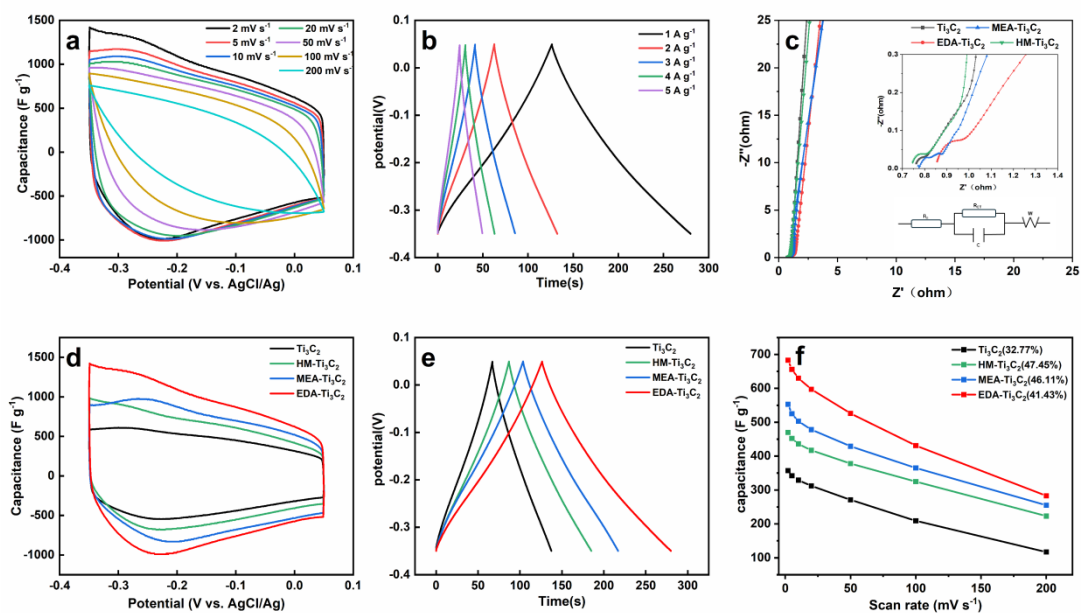
Figure 7. (a) CV of EDA-Ti$_3$C$_2$ at different scanning rates. (b) GCD of EDA-Ti$_3$C$_2$ at different current densities. (c) Nyquist plot in the frequency from 0.01 Hz to 100 kHz for Ti$_3$C$_2$, HM-Ti$_3$C$_2$, MEA-Ti$_3$C$_2$ and EDA-Ti$_3$C$_2$. Inserted are magnified plots at high frequency and the corresponding equivalent circuit model. (d) CV of Ti$_3$C$_2$, HM-Ti$_3$C$_2$, MEA-Ti$_3$C$_2$ and EDA-Ti$_3$C$_2$ at 2 mV s^{-1}. (e) GCD of Ti$_3$C$_2$, HM-Ti$_3$C$_2$, MEA-Ti$_3$C$_2$ and EDA-Ti$_3$C$_2$ at 1 A g^{-1}. (f) Capacitance retention at different scanning rates.

Based on the characterizations of amino-modified Ti$_3$C$_2$, electrochemical measurements are conducted with a three-electrode configuration, in which 1 M H$_2$SO$_4$, Ag/AgCl and activated carbon rod work as the electrolyte, reference and counter electrodes, respectively. We conducted CV measurements at different scan rates (**Figure 7a**, **Figure S5**). It is observed that there is no polarization phenomenon even at high scan rate of 200 mV s^{-1} within the voltage from -0.35 to 0.05 V, indicating excellent charge storage capacity and high-rate stability in MXene electrodes. In addition, GCD measurements are performed at various current densities (Figure 7b). All samples exhibit highly reversible redox reactions and efficient

charge-discharge processes.

Furthermore, EIS is conducted in the frequency range of 10^{-2} to 100 kHz. Figure 7c shows the Nyquist plot of Ti_3C_2, $HM-Ti_3C_2$, $MEA-Ti_3C_2$ and $EDA-Ti_3C_2$ electrodes. All EIS curves consist of a semicircular arc in the high-frequency region and a straight line in the low-frequency region. Generally, the diameter of the semicircular arc is related to the charge transfer resistance (R_{ct}), reflecting the transfer efficiency at the interface between the electrode and electrolyte. R_{ct} values are 0.0082, 0.035, 0.0094, and 0.0278 Ω for $HM-Ti_3C_2$, $MEA-Ti_3C_2$, $EDA-Ti_3C_2$ and Ti_3C_2, respectively. Small R_{ct} value indicates good conductivity and a large electroactive surface area in contact with H^+. The intercept on horizontal axis is related to the series resistance (R_s), which consists of the intrinsic resistance of the active material, the ionic resistance of the electrolyte, and the contact resistance between the electrode and the electrolyte. While the straight line reveals the influence of Warburg impedance due to capacitance characteristics and ion diffusion. R_s values are 0.737, 0.775, 0.844 and 0.754 Ω for $HM-Ti_3C_2$, $MEA-Ti_3C_2$, $EDA-Ti_3C_2$ and Ti_3C_2, respectively. $EDA-Ti_3C_2$ exhibited the highest internal resistance, which is consistent to the conductivity results in **Figure S3**.

The comparison of CV curves at 2 mV s^{-1} is shown in Figure 7d, and specific capacitances at different scan rates are listed in **Table S6**. Amino-modified Ti_3C_2 shows larger specific capacitance than Ti_3C_2 (357 F g^{-1}) at 2 mV s^{-1}. The reason may be due to large interlayer spacing in the modified Ti_3C_2, which restrains the self-stacking of nanosheets and ensures better contact between Ti_3C_2 and electrolyte ions. In addition, amino modification can provide more active sites, which enables fast redox reactions on the surface of modified Ti_3C_2 electrodes. It should be indicated that $EDA-Ti_3C_2$ exhibits the largest CV integration area with the largest specific capacitance of 683 F g^{-1}, which is much higher than other modified Ti_3C_2 electrodes ($HM-Ti_3C_2$: 470 F g^{-1}, $MEA-Ti_3C_2$: 553 F g^{-1}). The modification of Ti_3C_2 with EDA can provide the largest interlayer spacing with highest specific surface area, which helps to the electrolyte ion transport and diffusion, leading to more thorough reactions and improved electrochemical performance. In addition, there are more abundant

functional groups (-O, -OH, N-Q) in EDA-Ti$_3$C$_2$ resulted from the stronger electron-donating nature of EDA than HM and MEA, which ensures more active sites for the electrochemical reaction. In addition, for better understanding of the improvement by amino modification, specific capacitances from GCD curves are also given (**Table S7**). Bow two values from CV and GCD show the same trend with the amino modification of Ti$_3$C$_2$.

Figure 7e presents GCD curves at the current density of 1 A g^{-1} for all samples. All profiles exhibit quasi-triangle shapes, indicating good Coulombic efficiency and EDLC performance. The slight deviation from triangle shapes can be attributed to the pseudocapacitance caused by the redox-active N, O functional groups. Much longer discharge time of EDA-Ti$_3$C$_2$ than others suggests higher adsorption/desorption capacity for electrolyte ions in EDA-Ti$_3$C$_2$, which is beneficial for the capacitance. This agrees well with the larger CV integration area of EDA-Ti$_3$C$_2$. The rate performance is thus obtained in Figure 7f. Specific capacitances for amino-modified Ti$_3$C$_2$ exhibit much higher values than that of Ti$_3$C$_2$ in all scan rates. At 200 mV s^{-1}, Ti$_3$C$_2$ shows the lowest capacitance retention (32.77%) of the initial, while it is 47.46%, 46.11% and 41.43% for HM-Ti$_3$C$_2$, MEA-Ti$_3$C$_2$ and EDA-Ti$_3$C$_2$, respectively. The results indicate that the electrochemical performance of Ti$_3$C$_2$ is effectively improved by amino modification, which enhances the degree of electrode redox and ensures the reaction to be fully reversible even at high rates.

For high-performance supercapacitors, the cyclic stability is another crucial factor. **Figure S6** shows the cyclic stability at 50 mV s^{-1} for Ti$_3$C$_2$, HM-Ti$_3$C$_2$, MEA-Ti$_3$C$_2$ and EDA-Ti$_3$C$_2$, and the inset gives CV curves of the first and last cycles. All modified Ti$_3$C$_2$ exhibit excellent cyclic stability with the capacitance retention of over 97% after 10000 cycles, although it is a little bit lower than the Ti$_3$C$_2$. This may result from the unstable N-Q in modified Ti$_3$C$_2$, which is prone to breakage after long-term cycling, leading to irreversible redox reactions. To explain the cyclic stability of electrochemical performance, we investigate the morphology after cycling for all samples (**Figure S7**). As the electrode is prepared by coating the slurry onto copper foam, it's not possible to get their cross-section images after cycling. However, their

surface images still exhibit good morphology comparing with that before cycling as shown in Figure 1, which indicates well-preserved structure after cyclic stability. For example, EDA-Ti$_3$C$_2$ demonstrates very flat and smooth surface. Therefore, the amino-modified Ti$_3$C$_2$ can keep excellent cyclic stability.
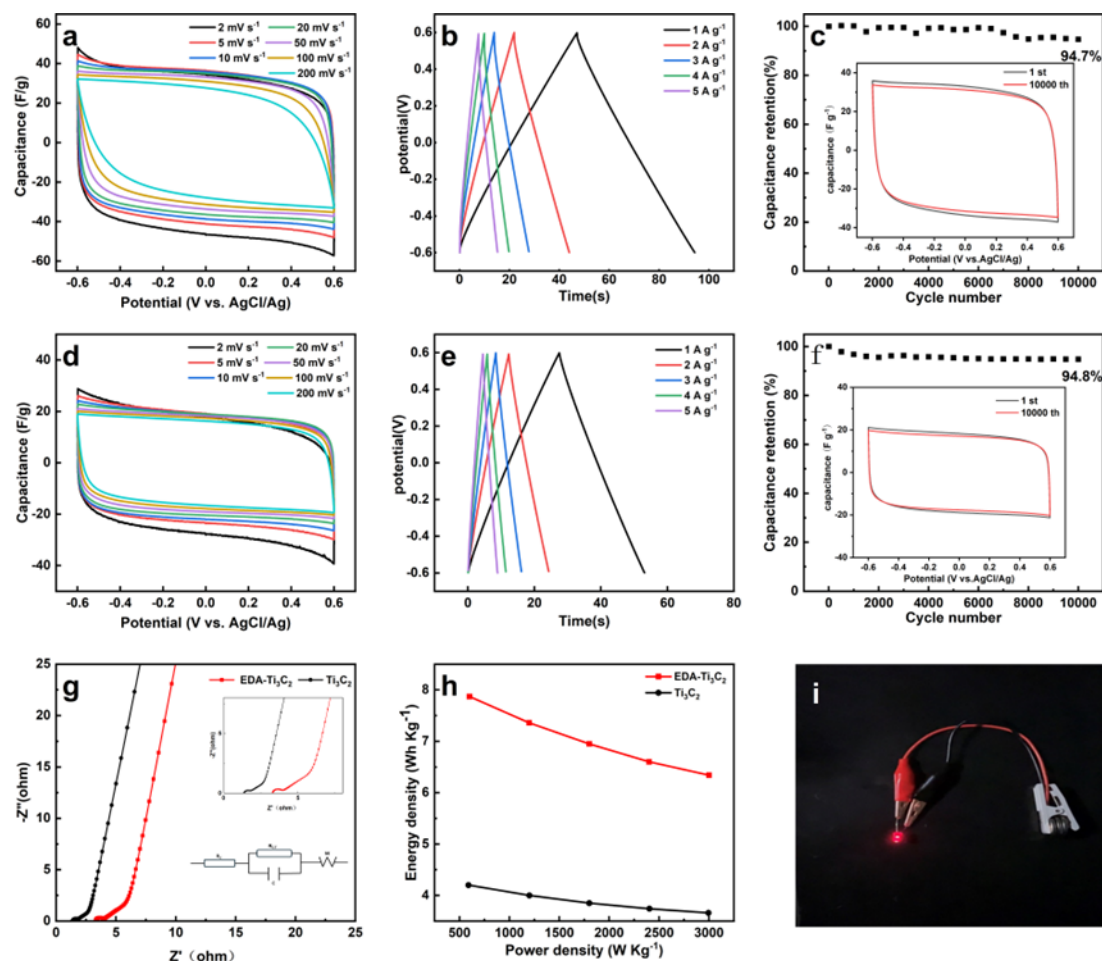
Figure 8. EDA-Ti$_3$C$_2$ symmetric supercapacitor (a) CV curves at scanning rates of 2-200 mV s^{-1}, (b) GCD curves at different current densities from 1 to 5 A g^{-1}, (c) Long-term cyclic tests from 1 to 10000 cycles at a scanning rate of 50 mV s^{-1}. Ti$_3$C$_2$ symmetric supercapacitor (d) CV curves at scanning rates of 2-200 mV s^{-1}, (e) GCD curves at different current densities from 1 to 5 A g^{-1}, (f) Long-term cyclic tests from 1 to 10000 cycles at a scanning rate of 50 mV s^{-1}. (g) EIS curves of EDA-Ti$_3$C$_2$ and Ti$_3$C$_2$ symmetric supercapacitors. Inserted are magnified plots at high frequency and the corresponding equivalent circuit model. (h) Different energy density and power density curves of the two symmetric supercapacitors. (i) Illumination of a red LED by connecting three EDA-Ti$_3$C$_2$ symmetric supercapacitors in series.

To understand the effect of amino modification on Coulombic efficiency, **Figure S8** gives Coulombic efficiency for both three-electrode and symmetric supercapacitors with Ti$_3$C$_2$ and EDA-Ti$_3$C$_2$. Amino-modified Ti$_3$C$_2$ is observed to exhibit much higher Coulombic efficiency than Ti$_3$C$_2$ at all current densities, with over 120% at 1A g^{-1} for

EDA-Ti$_3$C$_2$ as the electrode. For symmetric supercapacitors, the same conclusion can be obtained. Moreover, Coulombic efficiency is very stable for EDA-Ti$_3$C$_2$ with the value over 100% from 1 A g^{-1} to 5 A g^{-1}. Therefore, amino modification is an effective strategy to improve Coulombic efficiency of Ti$_3$C$_2$-based supercapacitors.

To validate the feasibility of amino-modified Ti$_3$C$_2$ electrodes in energy storage application, symmetric supercapacitor is fabricated with EDA-Ti$_3$C$_2$ as the electrode and 1 M Na$_2$SO$_4$ as the electrolyte, and the reference device is also prepared based on Ti$_3$C$_2$. The results are given in **Figure 8**.

All CV curves exhibit regular and symmetric rectangular shapes, which is consistent to that in three-electrode system. As the scan rate increases from 2 mV s^{-1} to 200 mV s^{-1}, CV curves still keep a good shape without any polarization (Figure 8a and d), demonstrating excellent rate capability and outstanding capacitance performance of the symmetric supercapacitors. GCD curves are plotted in Figure 8b and e. Within a wide voltage window of -0.6 to 0.6 V, which present approximately linear and symmetric profiles. Values of specific capacitance are calculated from formula (2), which are listed in **Table S8**. The EDA-Ti$_3$C$_2$ symmetric supercapacitor exhibits a specific capacitance of 39.3 F g^{-1} at 1 A g^{-1}, which is nearly twice that of the Ti$_3$C$_2$ symmetric supercapacitor (21 F g^{-1}). In addition, cyclic stability is evaluated with 10000 cycles by continuous CV measurements at 50 mV s^{-1}, which is shown in Figure 8c and 8f. The EDA-Ti$_3$C$_2$ symmetric supercapacitor demonstrates almost the same cyclic stability (94.7%) as that based on Ti$_3$C$_2$ (94.8%), indicating a long cycling lifetime and good electrochemical stability. Figure 8g gives the Nyquist plots in the frequency range of 10^{-2} to 100 kHz for both symmetric supercapacitors, from which the R$_s$ value is obtained to be 3.262 Ω and 1.341 Ω, and R$_{ct}$ value is 0.515 Ω and 0.293 Ω for symmetric supercapacitors based on Ti$_3$C$_2$ and EDA-Ti$_3$C$_2$, respectively. Due to the strong reducing nature of EDA, numerous oxygen-containing functional groups on the surface of EDA-Ti$_3$C$_2$ have been converted to nitrogen-containing functional groups, as confirmed by XPS analysis. Consequently, in Figure 8g, it is evident that the R$_s$ of EDA-Ti$_3$C$_2$ is significantly greater than that of Ti$_3$C$_2$, which is consistent with the conductivity values presented in Figure S3.

Furthermore, the effect of amino modification on energy density and power density of symmetric supercapacitors has been investigated (Figure 8h). The EDA-Ti$_3$C$_2$ device achieves maximum energy density of 7.87 W h Kg^{-1} at power density of 600 W Kg^{-1}. Even at an increased power density of 3000 W Kg^{-1}, the energy density still remains at 6.34 W h Kg^{-1}. Compared to the Ti$_3$C$_2$ device with a maximum energy density of 4.2 W h Kg^{-1}, the performance is improved by 87% with the introduction of EDA. In addition, when compared to previously reported MXene-based supercapacitors, such as, LT-Ti$_3$C$_2$T$_x$ (5.67 W h kg^{-1}, 589 W kg^{-1})[39]; MP-MX$_{1.5}$ (6.3 W h kg^{-1}, 56 W kg^{-1})[40] ; MoS$_2$-Ti$_3$C$_2$T$_x$ (5.1 W h kg^{-1}, 298 W kg^{-1})[41] and MnO$_2$/Ti$_3$C$_2$ (3.3 W h kg^{-1}, 2376 W kg^{-1})[42], the EDA-Ti$_3$C$_2$ device exhibits strong advantages in terms of its capacitance performance. Table S9 gives the comparison of energy density and power density of different electrodes. As shown in the real picture (Figure 8i), the EDA-Ti$_3$C$_2$ symmetric supercapacitor can provide a stable power source for a Light Emitting Diode (LED) indicator light. This confirms the reliability of amino-modified Ti$_3$C$_2$ symmetric supercapacitors as a promising power source in the future.

4. Conclusion

In summary, we propose the amino modification of Ti$_3$C$_2$ MXenes for high-performance supercapacitors. For three typical amino sources (HM, MEA and EDA), EDA provides the functionalized Ti$_3$C$_2$ with the highest nitrogen content (3.93%) and the lowest fluorine element content (5.77%). In addition, it ensures the largest interlayer spacing (13.96 Å) and the highest specific surface area (52.2 m^{2}g^{-1}), which helps to the electrolyte ion transport and diffusion. In addition, there are more abundant functional groups (-O, -OH, N-Q) in EDA-Ti$_3$C$_2$ resulted from the stronger electron-donating nature of EDA than HM and MEA, which ensures more active sites for the electrochemical reaction. As a result, the three-electrode supercapacitor based on EDA-Ti$_3$C$_2$ exhibits a high specific capacitance of 683 F g^{-1} at 2 mV s^{-1}. Even after 10,000 cycles, the capacitance retention remains above 97.3%. Furthermore, the symmetric supercapacitor with EDA-Ti$_3$C$_2$ electrode demonstrates a high energy

density of 7.87 W h Kg^{-1} at 600 W Kg^{-1}, and it could maintain an energy density of 6.34 W h Kg^{-1} at an increased power density of 3000 W Kg^{-1}, which is competitive to other similar reports. The functionalization demonstrates a facile and effective method to improve the capacitance properties of MXenes, which is closely related with the surface chemistry of MXenes. This work not only provides guidance for the selection of amino sources in surface modification strategies but also offers insights for the design of high-performance MXene-based supercapacitors in the future. However, the control of surface chemistry in MXenes is still a challenge, which definitely provides a variety of opportunities.

ACKNOWLEDGEMENTS

References

[1] X. Qin, J. Wan, Q. Zhang, Y. Zhang, H. Yu, S. Shi, Polyaniline-modified graphitic carbon nitride as electrode materials for high-performance supercapacitors, Carbon Lett. 33 (2023) 781–790. doi:10.1007/s42823-022-00459-y.

[2] M. Naguib, M. Kurtoglu, V. Presser, J. Lu, J. Niu, M. Heon, L. Hultman, Y. Gogotsi, M.W. Barsoum, Two-Dimensional Nanocrystals Produced by Exfoliation of Ti 3 AlC 2, Adv. Mater. 23 (2011) 4248–4253.

[3] Y. Wang, Y. Wang, Recent progress in MXene layers materials for supercapacitors: High-performance electrodes, SmartMat. 4 (2023) 1–35. doi:10.1002/smm2.1130.

[4] V. Armin, J. Rosen, Y. Gogotsi, The world of two-dimensional carbides and nitrides (MXenes), Science. 372 (2021) eabf1581. doi:10.1126/science.abf1581.

[5] J. Xu, T. Peng, Q. Zhang, H. Zheng, H. Yu, S. Shi, Intercalation Effects on the Electrochemical Properties of Ti3C2TxMXene Nanosheets for High-Performance Supercapacitors, ACS Appl. Nano Mater. 5 (2022) 8794–8803. doi:10.1021/acsanm.2c00632.

[6] C. Zhang, P. an Zong, Z. Ge, Y. Ge, J. Zhang, Y. Rao, Z. Liu, W. Huang, MXene-based wearable thermoelectric respiration sensor, Nano Energy. 118 (2023) 109037. doi:10.1016/j.nanoen.2023.109037.

[7] R. Ramírez-Grau, M. Cabrero-Antonino, H. García, A. Primo, MXene dots as photocatalysts for CO2 hydrogenation, Appl. Catal. B Environ. 341 (2024) 123316. doi:10.1016/j.apcatb.2023.123316.

[8] K.A. Nirmal, W. Ren, A.C. Khot, D.Y. Kang, T.D. Dongale, T.G. Kim, Flexible Memristive Organic Solar Cell Using Multilayer 2D Titanium Carbide MXene Electrodes, Adv. Sci. 10 (2023) 2300433. doi:10.1002/advs.202300433.

[9] J. Xu, T. Peng, X. Qin, Q. Zhang, T. Liu, W. Dai, B. Chen, H. Yu, S. Shi, Recent advances in 2D MXenes: preparation, intercalation and applications in flexible devices, J. Mater. Chem. A. 9 (2021) 14147–14171. doi:10.1039/d1ta03070a.

[10] N. Chen, H. Huang, Z. Xu, Y. Xie, D. Xiong, X. Chu, B. Gu, B. Zheng, W. Deng, H. Zhang, W. Yang, From high-yield Ti3AlCN ceramics to high-quality Ti3CNTx MXenes through eliminating Al segregation, Chinese Chem. Lett. 31 (2020) 1044–1048. doi:10.1016/j.cclet.2019.10.004.

[11] J. Choi, M.S. Oh, A. Cho, J. Ryu, Y.J. Kim, H. Kang, S.Y. Cho, S.G. Im, S.J. Kim, H.T. Jung, Simple Approach to Enhance Long-Term Environmental Stability of MXene Using Initiated Chemical Vapor Deposition Surface Coating, ACS Nano. 17 (2023) 10898–10905. doi:10.1021/acsnano.3c02668.

[12] N. Li, J. Huo, Y. Zhang, B. Ye, X. Chen, X. Li, S. Xu, J. He, X. Chen, Y. Tang, Y. Zhu, K. Ling, R. Zhu, Transition metal Carbides/Nitrides (MXenes): Properties, synthesis, functional modification and photocatalytic application, Sep. Purif. Technol. 330 (2024) 125325. doi:10.1016/j.seppur.2023.125325.

[13] J. Chen, Q. Jin, Y. Li, H. Shao, P. Liu, Y. Liu, P.L. Taberna, Q. Huang, Z. Lin, P. Simon, Molten Salt-Shielded Synthesis (MS3) of MXenes in Air, Energy Environ. Mater. 6 (2023) e12328. doi:10.1002/eem2.12328.

[14] M. Ghidiu, M.R. Lukatskaya, M.Q. Zhao, Y. Gogotsi, M.W. Barsoum, Conductive two-dimensional titanium carbide "clay" with high volumetric capacitance, Nature. 516 (2015) 78–81. doi:10.1038/nature13970.

[15] Q. Zhang, R. Fan, W. Cheng, P. Ji, J. Sheng, Q. Liao, Synthesis of Large-Area MXenes with High Yields through Power-Focused Delamination Utilizing Vortex Kinetic Energy, Adv. Sci. 9 (2022) 2202748.

[16] X. Liu, F. Xu, Z. Li, Z. Liu, W. Yang, Y. Zhang, H. Fan, Design strategy for MXene and metal chalcogenides / oxides hybrids for supercapacitors , secondary batteries and electro / photocatalysis, Coord. Chem. Rev. 464 (2022) 214544.

[17] J. Li, X. Yuan, C. Lin, Y. Yang, L. Xu, X. Du, J. Xie, J. Lin, Achieving High Pseudocapacitance of 2D Titanium Carbide (MXene) by Cation Intercalation and Surface Modification, Adv. Energy Mater. (2017) 1602725. doi:10.1002/aenm.201602725.

[18] P. Zhang, J. Li, D. Yang, R.A. Soomro, B. Xu, Flexible Carbon Dots-Intercalated MXene Film Electrode with Outstanding Volumetric Performance for Supercapacitors, Adv. Funct. Mater. 33 (2023) 2209918. doi:10.1002/adfm.202209918.

[19] L. Liu, H. Zschiesche, M. Antonietti, B. Daffos, N. V. Tarakina, M. Gibilaro, P. Chamelot, L. Massot, B. Duployer, P.L. Taberna, P. Simon, Tuning the Surface Chemistry of MXene to Improve Energy Storage: Example of Nitrification by Salt Melt, Adv. Energy Mater. 13 (2023) 2202709. doi:10.1002/aenm.202202709.

[20] Y. Luo, H. Yang, C. Ying, R. Wang, Z. Bo, J. Yan, K. Cen, K. Ostrikov, Plasma-Activated Solutions Regulate Surface-Terminating Groups Enhancing

Pseudocapacitive Ti3C2Tx Electrode Performance, Small. (2023) 2305383. doi:10.1002/smll.202305383.

[21]Z. Bo, Z. Huang, Z. Zheng, Y. Chen, J. Yan, K. Cen, H. Yang, K. (Ken) Ostrikov, Accelerated ion transport and charging dynamics in more ionophobic sub-nanometer channels, Energy Storage Mater. 59 (2023) 102797. doi:10.1016/j.ensm.2023.102797.

[22]J. Kong, H. Yang, X. Guo, S. Yang, Z. Huang, X. Lu, Z. Bo, J. Yan, K. Cen, K.K. Ostrikov, High-Mass-Loading Porous Ti3C2TxFilms for Ultrahigh-Rate Pseudocapacitors, ACS Energy Lett. 5 (2020) 2266–2274. doi:10.1021/acsenergylett.0c00704.

[23]R. Ibragimova, P. Erhart, P. Rinke, H.P. Komsa, Surface Functionalization of 2D MXenes: Trends in Distribution, Composition, and Electronic Properties, J. Phys. Chem. Lett. 12 (2021) 2377–2384. doi:10.1021/acs.jpclett.0c03710.

[24]J. Balamurugan, T.T. Nguyen, V. Aravindan, N.H. Kim, J.H. Lee, Flexible Solid-State Asymmetric Supercapacitors Based on Nitrogen-Doped Graphene Encapsulated Ternary Metal-Nitrides with Ultralong Cycle Life, Adv. Funct. Mater. 28 (2018) 1804663. doi:10.1002/adfm.201804663.

[25]J. Balamurugan, C. Li, V. Aravindan, N.H. Kim, J.H. Lee, Hierarchical Ni-Mo-S and Ni-Fe-S Nanosheets with Ultrahigh Energy Density for Flexible All Solid-State Supercapacitors, Adv. Funct. Mater. 28 (2018) 1803287. doi:10.1002/adfm.201803287.

[26]J. Balamurugan, T.T. Nguyen, V. Aravindan, N.H. Kim, S.H. Lee, J.H. Lee, All ternary metal selenide nanostructures for high energy flexible charge storage devices, Nano Energy. 65 (2019) 103999. doi:10.1016/j.nanoen.2019.103999.

[27]J. Balamurugan, P.M. Austeria, J.B. Kim, E.S. Jeong, H.H. Huang, D.H. Kim, N. Koratkar, S.O. Kim, Electrocatalysts for Zinc–Air Batteries Featuring Single Molybdenum Atoms in a Nitrogen-Doped Carbon Framework, Adv. Mater. 35 (2023) 2302625. doi:10.1002/adma.202302625.

[28]J. Yu, M. Zeng, J. Zhou, H. Chen, G. Cong, H. Liu, M. Ji, C. Zhu, J. Xu, A one-pot synthesis of nitrogen doped porous MXene/TiO2 heterogeneous film for high-performance flexible energy storage, Chem. Eng. J. 426 (2021) 130765. doi:10.1016/j.cej.2021.130765.

[29]F. Yang, D. Hegh, D. Song, J. Zhang, A nitrogenous pre-intercalation strategy for the synthesis of nitrogen-doped Ti3C2Tx MXene with enhanced electrochemical capacitance, J. Mater. Chem. A. 9 (2021) 6393–6401.

[30]R. Ma, X. Zhang, J. Zhuo, L. Cao, Y. Song, Y. Yin, X. Wang, G. Yang, F. Yi, Self-Supporting, Binder-Free, and Flexible Ti3C2TxMXene-Based Supercapacitor Electrode with Improved Electrochemical Performance, ACS Nano. 16 (2022) 9713–9727. doi:10.1021/acsnano.2c03351.

[31]M. Naguib, O. Mashtalir, M.R. Lukatskaya, B. Dyatkin, C. Zhang, V. Presser, Y. Gogotsi, M.W. Barsoum, One-step synthesis of nanocrystalline transition metal oxides on thin sheets of disordered graphitic carbon by oxidation of MXenes, Chem. Commun. 50 (2014) 7420–7423. doi:10.1039/c4cc01646g.

[32]A. Sarycheva, Y. Gogotsi, Raman Spectroscopy Analysis of the Structure and

Surface Chemistry of Ti3C2T MXene, Chem. Mater. 32 (2020) 3480–3488. doi:10.1021/acs.chemmater.0c00359.

[33] Y. Tan, C. Xu, G. Chen, Z. Liu, M. Ma, Q. Xie, N. Zheng, S. Yao, Synthesis of ultrathin nitrogen-doped graphitic carbon nanocages as advanced electrode materials for supercapacitor, ACS Appl. Mater. Interfaces. 5 (2013) 2241–2248. doi:10.1021/am400001g.

[34] N.Q. Tran, B.K. Kang, M.H. Woo, D.H. Yoon, Enrichment of pyrrolic nitrogen by hole defects in nitrogen and sulfur co-doped graphene hydrogel for flexible supercapacitors, ChemSusChem. 9 (2016) 2261–2268. doi:10.1002/cssc.201600668.

[35] J. Low, L. Zhang, T. Tong, B. Shen, J. Yu, TiO 2 / MXene Ti 3 C 2 composite with excellent photocatalytic CO 2 reduction activity, J. Catal. 361 (2018) 255–266. doi:10.1016/j.jcat.2018.03.009.

[36] P. Xu, H. Xiao, X. Liang, T. Zhang, F. Zhang, C. Liu, B. Lang, Q. Gao, A MXene-based EDA-Ti3C2Tx intercalation compound with expanded interlayer spacing as high performance supercapacitor electrode material, Carbon N. Y. 173 (2020) 135–144. doi:10.1016/j.carbon.2020.11.010.

[37] A. Amiri, Y. Chen, C. Bee, M. Naraghi, Porous nitrogen-doped MXene-based electrodes for capacitive deionization, Energy Storage Mater. 25 (2020) 731–739. doi:10.1016/j.ensm.2019.09.013.

[38] X. Zheng, M. Yuan, D. Guo, C. Wen, X. Li, X. Huang, H. Li, G. Sun, Theoretical Design and Structural Modulation of a Surface-Functionalized Ti 3 C 2 T x MXene- Based Heterojunction Electrocatalyst for a Li − Oxygen Battery, ACS Nano. 16 (2022) 4487–4499.

[39] X.H. Pan, N.M. Shinde, M. Lee, D. Kim, K.H. Kim, M. Kang, Controlled nanosheet morphology of titanium carbide Ti3C2Tx MXene via drying methods and its electrochemical analysis, J. Solid State Electrochem. 24 (2020) 675–686. doi:10.1007/s10008-020-04495-4.

[40] Z. Fan, Y. Wang, Z. Xie, X. Xu, Y. Yuan, Z. Cheng, Y. Liu, A nanoporous MXene film enables flexible supercapacitors with high energy storage, Nanoscale. 10 (2018) 9642–9652. doi:10.1039/c8nr01550c.

[41] W. Hou, Y. Sun, Y. Zhang, T. Wang, L. Wu, Y. Du, W. Zhong, Mixed-dimensional heterostructure of few-layer MXene based vertical aligned MoS2 nanosheets for enhanced supercapacitor performance, J. Alloys Compd. 859 (2021) 157797. doi:10.1016/j.jallcom.2020.157797.

[42] W. Liu, Z. Wang, Y. Su, Q. Li, Z. Zhao, F. Geng, Molecularly Stacking Manganese Dioxide / Titanium Carbide Sheets to Produce Highly Flexible and Conductive Film Electrodes with Improved Pseudocapacitive Performances, Adv. Energy Mater. 7 (2017) 1602834. doi:10.1002/aenm.201602834.